Palaeogeography, Palaeoclimatology, Palaeoecology 461 (2016) 109–121

Contents lists available at ScienceDirect

Palaeogeography, Palaeoclimatology, Palaeoecology

journal homepage: www.elsevier.com/locate/palaeo

A multi-proxy stalagmite record from northwestern Namibia of regional drying with increasing global-scale warmth over the last 47 kyr: The interplay of a globally shifting ITCZ with regional currents, winds, and rainfall

L. Bruce Railsback [a,*], George A. Brook [b], Fuyuan Liang [c], Eugene Marais [d], Hai Cheng [e,f], R. Lawrence Edwards [f]

[a] Department of Geology, University of Georgia, Athens, GA 30602-2501, USA
[b] Department of Geography, University of Georgia, Athens, GA 30602-2502, USA
[c] Department of Geography, Western Illinois University, 1 University Circle, Macomb, IL 61455, USA
[d] Entomology Centre, National Museum of Namibia, P.O. Box 1203, Windhoek, Namibia
[e] College of Global Environmental Change, Xi'an Jiaotong University, Xi'an, Shaanxi 710049, China
[f] Department of Geology and Geophysics, University of Minnesota, Minneapolis, MN 55455, USA

ARTICLE INFO

Article history:
Received 4 April 2016
Received in revised form 9 August 2016
Accepted 11 August 2016
Available online 13 August 2016

Keywords:
Namibia
Paleoclimate
Pleistocene
Holocene
Savanna
Stalagmite

ABSTRACT

Stalagmite Orum-1 from a cave near Orumana in northwestern Namibia provides a multi-proxy record of regional drying with increasing global-scale warmth over the last 47 kyr, in a region with few long well-dated location-specific paleoclimate records. Data from Stalagmite Orum-1 include carbon and oxygen stable isotope ratios, proportions of aragonite and calcite, pronouncedly differing petrographic fabrics, positions of layer-bounding surfaces, variation in layer-specific width, and changes in layer thickness, all of which combine to support change from wetter to drier conditions. Combined with fourteen U-Th ages, they suggest that climate was wetter in northwestern Namibia during globally cold MIS 3 than it is today, and with more grass than is present today. The climate at Orumana became drier during the deglacial transition after the Last Glacial Maximum, but carbon isotope data indicate that C_4 grasses persisted. In the Holocene, even greater aridity led to a reduction in grass cover and to the present C_3-dominated vegetation. Hiatuses in Stalagmite Orum-1 suggest even drier conditions during the Bølling-Allerød and during the early Holocene thermal maximum.
Wetter conditions at Orumana during glacial times may have resulted from movement of the Intertropical Convergence Zone southward, in a shift that was significant west of longitude 13°E but perhaps less significant east of that line. It may have been accompanied by a lesser southward shift of the Angola-Benguela Front at sea and/or the Inter-Ocean Convergence Zone on land, leading to increased rainfall in northern Namibia (but perhaps not farther south). Extrapolation from the present to warmer conditions in the next century would suggest that further drying in northern Namibia and southern Angola may occur.

1. Introduction

Three factors combine to make studies of past climate in southern Africa important both to human survival and to science. First, the dry climate of the region continually imperils agriculture and animal husbandry, which are critical to human sustenance across the region, and the scarcity of water limits economic development (e.g., Lange, 1997). Secondly, the sharp contrasts in rainfall across the region, both with regard to amount and seasonality, mean that shifts in climatic belts can have great impact on climate at any one location. Consequently, southern Africa is ranked as the region of the world likely to be most impacted by desertification in the next two decades (DARA and the Climate Vulnerability Forum, 2010). Thirdly, past climate change in southern Africa, and especially southwestern Africa, is the subject of explicit disputes about change in the region over the past tens of thousands of years, and most intensely with regard to the Last Glacial Maximum (e.g., Heine et al., 2014, p. 174). Conflicting results from different locations make any synthesis problematical, and there is commonly disagreement between ages generated by radiocarbon dating of organic matter, ages generated by radiocarbon dating of carbonate, and ages from sediments dated using optically-stimulated luminescence (OSL) (Brook et al., 2011; Stone et al., 2010). Furthermore, most interpretations of the region's past climate rely on proxy information from marine sediment cores that receive signals from environmentally diverse landscapes upwind and upstream from the cores themselves

* Corresponding author.
E-mail address: rlsbk@gly.uga.edu (L.B. Railsback).

http://dx.doi.org/10.1016/j.palaeo.2016.08.014
0031-0182/

(e.g., Stuut et al., 2002; Dupont and Wyputta, 2003) (see also Lim et al., 2016, pp. 198 and 203). These factors combine to emphasize the importance of precisely-dated single-point records of past climate from the continent itself.

In light of the above considerations, this paper presents a paleoclimate record from an unusual stalagmite from a cave near Orumana in northwestern Namibia. Stalagmite Orum-1 provides a discontinuous but useful record of climate change over the last 47 kyr, with precise and reliable ages generated by U-Th dating. The stalagmite's characteristics vary greatly in response to what appears to have been considerable change in wetness of climate. Furthermore, the stalagmite's record of drying and aridification from the globally cooler Late Pleistocene environment to warmer Holocene conditions suggests that even drier conditions could develop if climate continues to warm over the next century.

2. Setting

2.1. The landscape and environment of northwestern Namibia

Orumana Cave is near Orumana Mission Station (18° 15.42′ S; 13° 53.68′ E), which is about 25 km SSE from Opuwo or Opuvo, in the northern part of the Kunene Region of northwestern Namibia, at an elevation of about 1450 masl. It is roughly 170 km inland from the Atlantic coast, in the rugged Joubert Mountains that constitute the Kaokoveld Karst terrain (Irish et al., 2001). Orumana is in the upper catchment of the Hoarusib River, which drains toward the Atlantic Ocean and which, although ephemeral, "reaches the sea almost every year" (Srivastava et al., 2005).

Orumana lies in the austral tropical summer rainfall zone (Fig. 1) and has an average annual rainfall of about 300 mm/yr falling mainly from October to April. The quantity of summer rain diminishes progressively toward the south until it transitions into a winter rainfall zone much farther south. Rainfall increases towards the north to where precipitation during the equinoxes dominates at the equator (Transect 1–9 of Fig. 1).

Orumana lies just south of the latitude of the Atlantic Ocean's Angola-Benguela Front (ABF), where the cold Benguela Coastal Current coming from the south meets the warm Angola Current coming from the north (Fig. 2). The 21 °C isotherm of sea-surface temperature, midway between the 15 °C temperature of the Benguela Coastal Current and 27 °C of the Angola Current, moves north and south from 13°S in austral winter to 17°S in austral summer (Fig. 4.1.1 of Veitch, 2002). When the Angola Current breaches the Front and moves farther south, evaporation from its surface causes more rain to fall on the lands to the east (Rouault et al., 2003). The general position of the Front at sea matches that of the northern margin of the Namib Desert on land (Fig. 2).

Orumana is also located just south of a convergence of air masses, the Inter-Ocean Convergence Zone (IOCZ), which has also been called the "Congo Air Boundary" or "Zaire Air Boundary" (Fig. 2). The IOCZ is the convergence of air masses from the Indian Ocean and tropical Atlantic Ocean (van Heerden and Taljaard, 1998). During summer, and thus during the wet season, the IOCZ runs almost west-east just north of the border between Namibia and Angola, with winds off the nearby tropical Atlantic Ocean on the north (Angolan) side and winds from the distant Indian Ocean on the south (Namibian) side. Offshore, and to the south of the IOCZ, is a nearby semi-permanent coastal high-pressure cell over the cold Benguela upwelling areas along the Namibian coast. The IOCZ coincides with a steep gradient in annual rainfall, with more rainfall to the north associated with tropical Atlantic moisture as opposed to drier air to the south, and this southward migration of the IOCZ brings more rain to northern Namibia (Tyson, 1986; Mattes and Mason, 1998).

Within the austral summer rainfall zone, rainfall increases inland from the coast to Orumana and onward to southeastern Angola (Transect A-C of Fig. 1), leading to climatic zones that change over small distances near Orumana. In the updated Köppen-Geiger climate classification of Kottek et al. (2006), Orumana lies at the boundary of BSk (cold arid steppe, because of the prevailing influence of the coastal high-pressure inversion) and Cwb (warm temperate climate with dry winter and warm summer) (Fig. 3). Only 50 km to the northeast is Cwa (warm temperate climate with dry winter and hot summer) and only about 70 km to the southeast is BSh (hot arid steppe) (Fig. 3). Rainfall increases abruptly to the northeast, doubling from 300 mm annually to 600 mm over a distance of only 210 km (Fig. 2).

This progression of increasing rainfall and wetter climate from west-southwest to east-northeast through Orumana largely accounts for the transition from the hyperarid Namib Desert along the coast to a complex semidesert/savanna mosaic at Orumana as part of the Kaokoveld

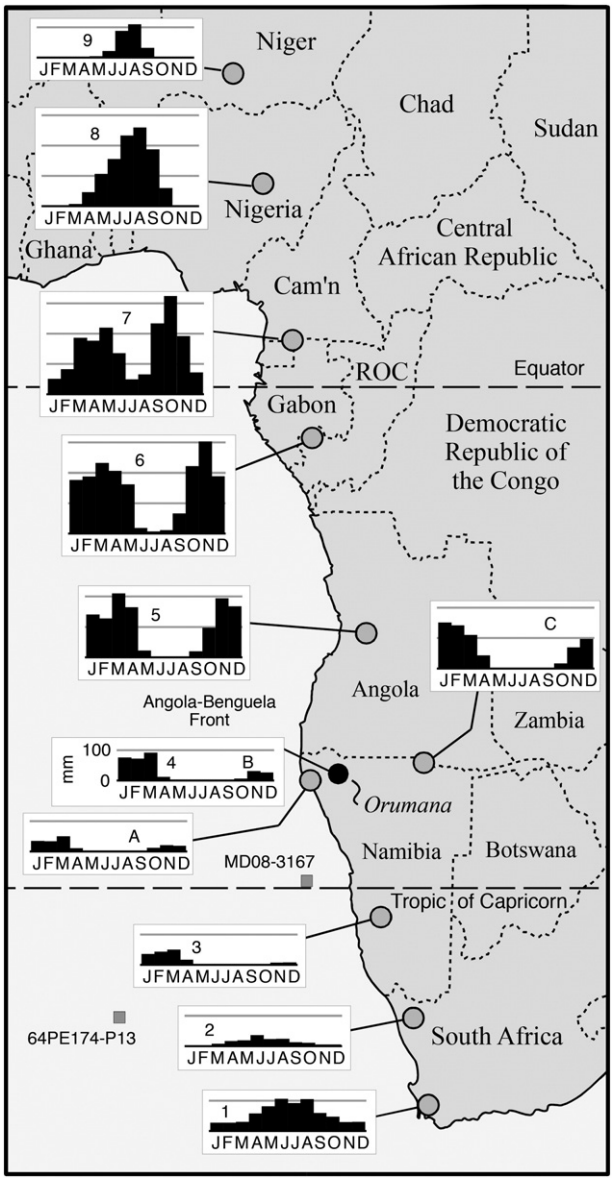

Fig. 1. Map showing the location of Orumana in northwestern Namibia (black-filled circle). Histograms show average monthly rainfall at locations marked with circles; the vertical scale for all is the same as that shown for Orumana. Histograms 1 to 9 provide a south-to-north transect; Histograms A to C provide a transect from the Atlantic coast inland as discussed in Section 2.1. From south to north, climate zones proceed from austral winter rainfall to austral summer rainfall to equatorial equinoctial rainfall to boreal summer rainfall. Histograms of atmospheric precipitation covering the period from 1961 to 1990 are from the gridded data of New et al. (1999) as presented at the World Bank's Climate Change Knowledge Portal at sdwebx.worldbank.org/climateportal/index.cfm?page=global_map. Squares mark locations of marine cores discussed in Sections 5.1 and 5.2.

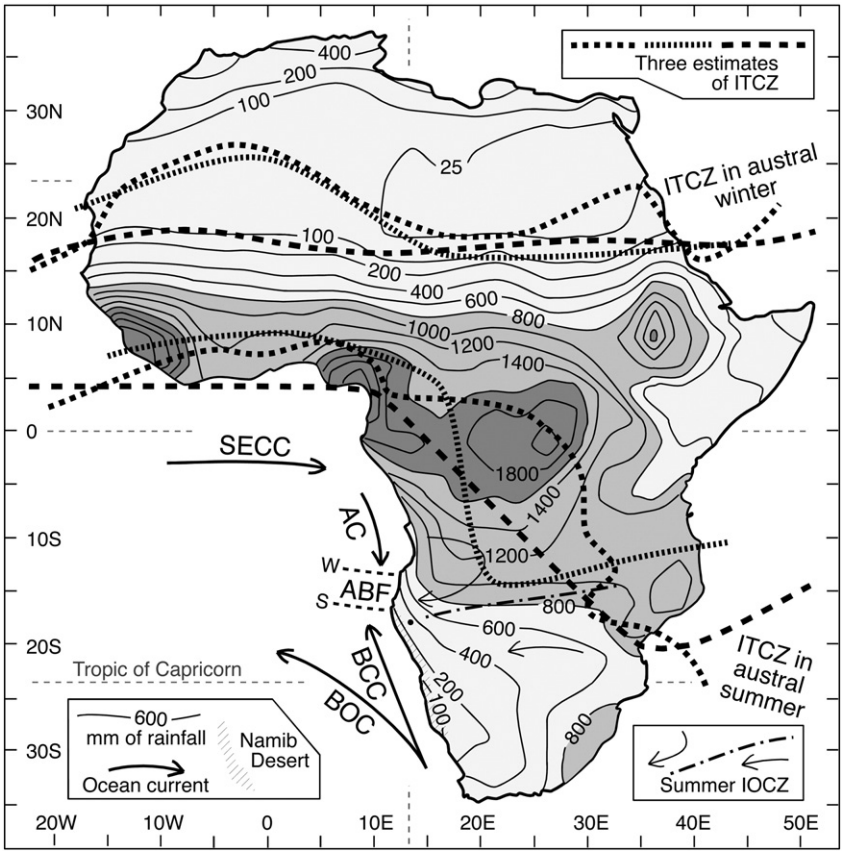

Fig. 2. Map of Africa with isohyets for annual rainfall from the Global Precipitation Climatology Project (GPCP) of the U.S. National Aeronautics and Space Administration (NASA). The filled circle in southwestern Africa, at 18°S, 14°E, is the location of the Orumana stalagmite (Section 2). Bold lines show the positions of the Intertropical Convergence Zone in austral winter and austral summer as shown by Wang (2009) (broadly dashed line), Dupont et al. (2008) (finely dashed or coarsely dotted line) and Nicholson (2009) (finely dotted line). Currents in the southeastern Atlantic are the Southern Equatorial Counter Current (SECC), Angola Current (AC), and Benguela Current (BC). ABF is the Angola-Benguela Front in austral winter (W) and austral summer (S). IOCZ is the Inter-Ocean Convergence Zone of winds from Indian and Atlantic Oceans, taken from Fig. SD.3 of van Heerden and Taljaard (1998). The dashed line at 13°E is a general boundary discussed in Section 5.3.2. Currents and position of the ABF are from Veitch (2002); Benthien et al. (2005), and Dupont et al. (2008).

Centre of Endemism (Craven, 2009) and thence to savanna just east of Orumana (White, 1983; UNEP, 2010). Grass cover increases abruptly from <10% in the semidesert belt to 25–75% in the savanna and floodplains of the Cuvelai drainage system (Mendelsohn et al., 2002). Fig. 10.4 of Ehleringer (2005) shows that, to the north and east of Orumana, C_4 grasses make up 60 to 100% of the grasses present, and Fig. 4 of Still et al. (2003) indicates that >90% of the vegetation there is C_4 plants (although the region is not a grassland and is instead a mopane savanna). Thus the region can be divided along a NNW-SSE line, with vegetation rich in C_4 grasses in the wetter region to the east of Orumana and a drier region with a much smaller proportion of C_4 plants at Orumana and to the west (Fig. 3).

Around the cave itself, the vegetation on the plateau consists predominantly of a variety of trees and large shrubs typical of the wetter parts of the mountainous Kaoko Escarpment zone from ca. 15°S in southwestern Angola to ca. 20°S in Namibia (Craven, 2009), i.e. the northern part of the Woodland Savanna ecoregion (Mendelsohn et al., 2002). The open woodland is dominated by *Commiphora crenatoserrata*, *Kirkia acuminata* and *Euphorbia* spp. trees with scattered *Terminalia prunioides*, *Commiphora* spp. and *Dichrostachys cinerea* shrub and sparse C_4 grasses. A range of trees and shrubs occur around the cave that are rare on the plateau, e.g. *Ficus cordata*, *Sterculia africana*, *Combretum apiculatum*, *Boscia albitrunca*, *Grewia* sp. and *Ximenia* sp.

To summarize, Orumana lies in a south-to-north gradient of increasing rainfall in which a dynamic boundary at sea (the ABF) can significantly change rainfall to give either arid or more hospitable climate, with an analogous frontal boundary on land (the IOCZ), *and* it lies at a boundary in a west-to-east transition from desert to savanna, with greater rainfall to the east. This location makes significant climate change through time likely, and it makes a paleoenvironmental record from Orumana important in understanding the region's climate history.

2.2. The cave at Orumana

The cave at Orumana is developed in cherty dolostones of the Neoproterozoic Tsumeb Subgroup (Martini et al. (1990), which is the uppermost subdivision of the Otavi Group of the Damara Supergroup (Hoffmann and Prave, 1996; Hoffman et al., 1998; Miller, 2008). The dolostone is distinctly bedded, with layers dipping slightly to the east. Martini et al. (1990) and Martini et al. (1999) provide maps of the cave, and Photo 2 of Martini et al. (1999) shows a large portion of the cave's interior, with many stalactites hanging from a broad ceiling. Despite the abundance of stalactites, stalagmites are very rare (Martini et al., 1999), suggesting that most dripwater evaporates on the cave's ceiling rather than falling to the floor. Little else is known about the hydrology of this remote cave. Martini et al. (1999) pointed out that, of the caves in Kaokoland, Orumana alone has been known to and visited from time to time by the indigenous peoples.

Martini et al. (1990) pointed out that the cave at Orumana cannot be the result of collapse, both because there are not sufficient large blocks on the floor for collapse to have been significant and because the walls of the cave are smooth and suggest a dissolutional origin. However, at present the cave is so dry that Martini et al. (1990) specifically reported that, "at one spot on the floor a drip forms a small pool of water", with the rest presumably dry. Thus the cave itself suggests much wetter

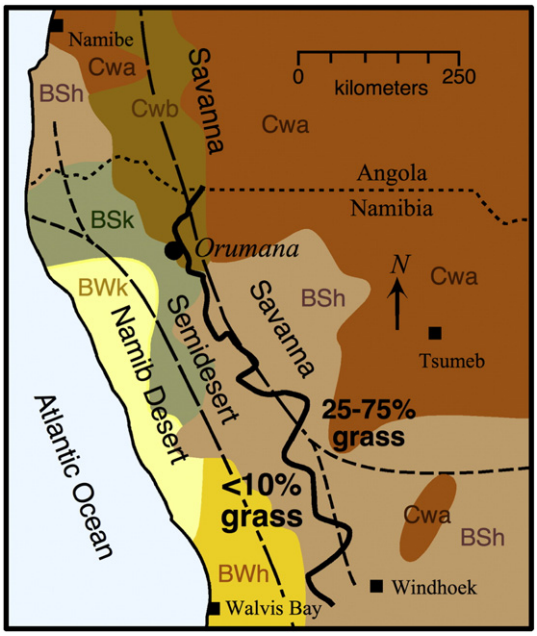

Fig. 3. Map of northern Namibia and southern Angola showing vegetation and climate zones. Dashed boundaries between vegetation zones of desert, semidesert, and savanna are generalized from U.S. Central Intelligence Agency (1986) and UNEP (2010), which was based on Chi-Bonnardel (1973); finer dashed branches show variants depending on source. The bold line is the boundary between the region with little grass cover and the region with a considerable grass cover (labeled in bold) as shown by the Atlas of Namibia Project (2002). The latter line coincides with the western boundary of regions rich in C_4 vegetation shown in Fig. 10.4 of Ehleringer (2005) and Fig. 4 of Still et al. (2003). Colored fields and three-letter codes indicate regions in the Köppen-Geiger classification of climate as presented by Kottek et al. (2006).

Fig. 4. Scanned image of a vertical section of Stalagmite Orum-1. In the sketch at upper right, solid lines outline the four growth periods discussed in Section 4.2, and dotted lines indicate the four major Type L surfaces. Fig. 6 shows the exterior of the top of the stalagmite, and Fig. 8 shows the area at lower right in more detail.

conditions at some point in the past when the water table was sufficiently high to cause the dissolution that created the present cavity.

Stalagmite Orum-1 (Fig. 4) was collected in 2004 from the top of a large, prominent stalagmitic complex on the floor of the cave. Stalagmite Orum-1 protruded from the top of the complex, some 6 m above the floor of the cave.

3. Methods

3.1. U-Th ages

Positions in Stalagmite Orum-1 were indexed along the growth axis, which includes a protrusion that deviates from the vertical axis of the stalagmite (Fig. 5). Fourteen samples for U-Th radiometric dating were drilled from Stalagmite Orum 1. Thirteen of these were along the growth axis, and the fourteenth sample was drilled from the flank of the stalagmite, just below a prominent surface of physical breakage, in order to determine a minimum age for the time when the stalagmite was broken. All samples were drilled to follow single layers except Sample B in Period III (see Section 4.2), where abundant detrital material required drilling along multiple laminae to obtain a large enough sample for dating, so that the age of Sample B is the average of a slightly longer time period than is the case for the other samples. One sample (OR-6) yielded anomalous $\delta^{234}U$ values and was replaced by sample OR-6R, which gave almost the same age but with $\delta^{234}U$ values more similar to those obtained from the analysis of the other samples.

All fourteen samples were dated by inductively coupled plasma mass spectrometry (ICP-MS) in the Stable Isotope Laboratory of the University of Minnesota using techniques described in Edwards et al. (1987) and Cheng et al. (2000). Ages were calculated using half-lives from Cheng et al. (2000) and are reported with analytical errors of 2σ of the mean (Table 1). Corrections for detrital Th were made by assuming a $^{230}Th/^{232}Th$ ratio equal to the average for Earth's crust, (4.4×10^{-6}); the isochron method was not used because multiple sampling along individual depositional laminae would have been difficult in the stalagmite examined. The approach we used is preferable because the coralloidal structure of the stalagmite precludes detailed correlation, so that the corrections, which ranged from 32 to 770 years, are irrelevant to the broad correlations considered in Section 5 (as is shown in the figure on which those correlations are made). Even for the Holocene, where corrections are proportionately greatest, the magnitudes of the corrections affect the ages and conclusions very little because the most precise designation of age for Period IV in this paper is "Late Holocene".

3.2. Methods for stable isotopes, mineralogy and growth layer geometry

Carbon and oxygen stable isotope analyses were performed using a method modified from that of McCrea (1950). Samples weighing 5 to 10 mg were reacted under vacuum in 100% phosphoric acid at 50 °C. The resulting CO_2 was extracted on a conventional vacuum line and analyzed on Finnigan MAT Delta E and MAT 252 mass spectrometers. Laboratory standards were prepared and analyzed with each batch of samples. These standards have been calibrated to NBS-19 ($\delta^{13}C = +1.95$, $\delta^{18}O = -2.2$‰ relative to VPDB) and NBS-18 ($\delta^{13}C = -5.0$ and $\delta^{18}O = -23.0$‰ relative to VPDB). Isotopic results from samples were normalized to the lab standards using a two-point scale, so that all $\delta^{13}C$ and $\delta^{18}O$ values reported here are relative to VPDB. The 2-sigma error of the combined extraction and analysis was 0.04‰ for $\delta^{13}C$ and 0.05‰ for $\delta^{18}O$.

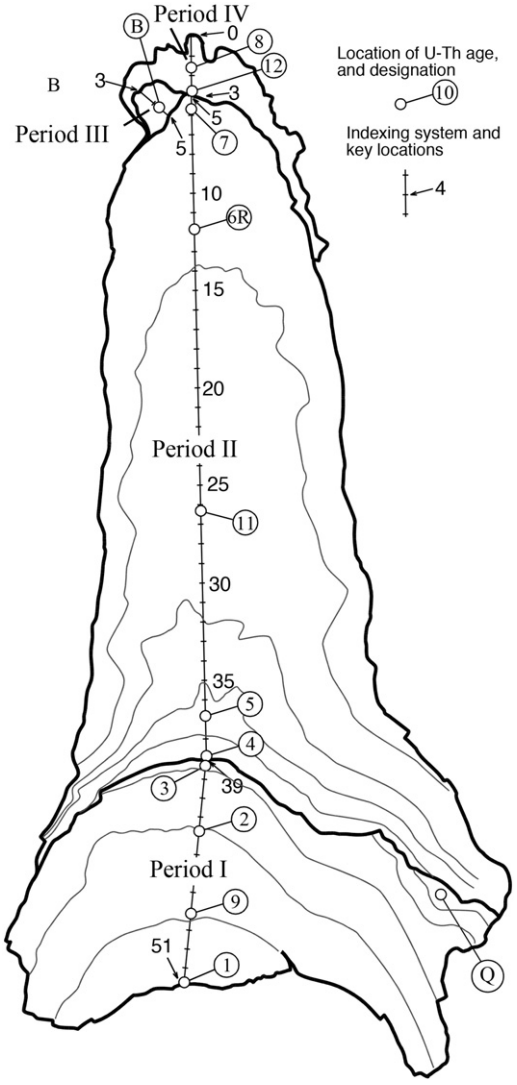

Fig. 5. Sketch of Stalagmite Orum-1 showing the indexing system (cm) and the position of samples taken for radiometric dating, as discussed in Section 3.1. Note that, from 3 cm to 5 cm, the indexing system takes into account a lateral protrusion that was not deposited along the vertical axis of the stalagmite (Period III). Also note that Sample Q for dating was taken from the flank, not the growth axis, to determine how long deposition continued before the stalagmite was broken at the boundary between Periods I and II. Analysis of Sample Q reveals that deposition continued for at least 15 ka after deposition of the material in Sample 3 but before the stalagmite was broken (Table 1).

Mineralogy of powdered samples was determined using a Bruker D8 X-ray Diffractometer in the Department of Geology of the University of Georgia. Samples were scanned from 10 to 65°2Θ using $Co_{K\alpha}$ radiation.

Layer-specific width was determined using the method shown in Fig. 2 of Sletten et al. (2013) and Fig. 3 of Railsback et al. (2014). The angle used was 25°, intermediate between the values of 10° and 33° used by Sletten et al. (2013) and Railsback et al. (2014), respectively.

4. Results

4.1. Form of Stalagmite Orum-1

Stalagmite Orum-1 has a vertical extent of 51 cm along its growth axis. It has a wide base, in that the lower third of the stalagmite is about 25 cm in diameter. In contrast, the upper two thirds of the stalagmite are about 10–15 cm in diameter, becoming smaller upward (Fig. 4).

The exterior of the upper quarter of Stalagmite Orum-1 has many protrusions roughly 1 cm in diameter and 1 cm in height (Fig. 6). These digitate protrusions are known to speleologists as “coralloids” (Caddeo et al., 2015) or “cave popcorn” (Hill and Forti, 1997). The vertical section of the stalagmite cut along its growth axis additionally reveals coralloids in much, but not all, of the interior of the stalagmite (Fig. 4).

4.2. Periods of growth in, and age model for, Stalagmite Orum-1

Stalagmite Orum-1 grew during four distinct periods that are separated by prominent surfaces, two of which resulted from breakage of the stalagmite (Figs. 4 and 7). The lowermost and therefore earliest period (Period I) lies below a surface of breakage that truncates many layers (Fig. 8). The break crosses the growth axis of the stalagmite 39 cm from the top and extends across the stalagmite at its widest point, suggesting that a sizeable upper section of the stalagmite was broken off. U-Th ages show that the material below the break was deposited from 47 ka to at least 24 ka (Table 1), although the stable isotope record for Period I extends only from 47 to 38 ka because axial deposits younger than 38 kyr were broken off. The break may have resulted from the activity of humans visiting the cave (Martini et al., 1999) or have been triggered by natural roof-fall.

Period II extends from 39 cm below the top of the stalagmite to just 5 cm below the top, and thus it represents most of the stalagmite's vertical extent (Figs. 4 and 5). The upper boundary of Period II is a dark layer that extends across the top of the stalagmite with no evidence of breakage associated with it, although some layers were broken off one side of the stalagmite prior to deposition of the dark layer. U-Th ages for Period II range from 20 to 15 ka (Fig. 7; Table 1).

Period III is represented by a small pinnacle, or knob, to one side of the main stalagmite growth axis (Figs. 4–6). It extends 2 cm from the underlying material of Period II. It is underlain by about one third of the dark layer that caps Period II and is overlain by about two thirds of that layer. A U-Th age of 13.7 ka for Sample B provides an age for Period III, as discussed in Section 3.1. A surface of breakage within Period III, recognizable only in thin section, suggests that it may represent multiple discrete time periods, and the upper boundary of Period III appears to be a broken surface.

Period IV constitutes the uppermost 3 cm of the stalagmite (Fig. 4). U-Th ages in Period IV range from ca. 1.0 to 0.9 ka (Fig. 7; Table 1). The top surface of Period IV, the top of the stalagmite, shows no evidence of breakage.

4.3. Layer-bounding surfaces

Like almost all stalagmites, Stalagmite Orum-1 contains Type L surfaces (surfaces below which layers thin and cover a smaller area of the stalagmite, suggesting drier conditions) and Type E surfaces (surfaces at which underlying layers have undergone corrosion and dissolutional erosion) (Railsback et al., 2013) (Figs. 4 and 9). Four of the six Type L surfaces recognized in Stalagmite Orum-1 are in Period II. In contrast, Type E surfaces are common in Period I. Those Type E surfaces rarely cut through multiple layers and instead only suggest corrosion of tops of individual layers (Fig. 9), suggesting seasonally wet conditions rather than major wet intervals.

4.4. Fabrics and layer thickness

The petrographic fabric of Stalagmite Orum-1 ranges from simple domal laminae to coralloids, with the coralloids best-developed at the stalagmite's crest rather than its flanks. Period I consists mostly of domal laminae, whereas Periods II to IV are largely coralloidal. Layer thickness is very difficult to measure in the coralloidal intervals, for two reasons: the changing attitude of layers means that observations in sections are mostly apparent thicknesses that are greater than actual thicknesses, and actual thickness of an individual layer in coralloids commonly varies along the length of the layer (Caddeo et al., 2015).

Table 1
U-Th dating results for Stalagmite Orum-1.

Distance								Uncorrected	Corrected	
Sample from top		weight	^{238}U (ppb)	^{232}Th (ppt)	$\delta^{234}U$ measured[a]	$[^{230}Th/^{238}U]$ activity[b]	$[^{230}Th/^{232}Th]$ (ppm)[c]	Age (yrs)	Age[d] (yrs)	$\delta^{234}U_{initial}$ corrected[a]
ID	(cm)	(g)								
OR-8	1.7	0.0930	1763.3 ± 3.8	8724 ± 28	1124.0 ± 3.1	0.02045 ± 0.00030	68 ± 1	1053 ± 15	986 ± 37	1127.1 ± 3.1
OR-12	3.0	0.1500	436.4 ± 1.5	3016 ± 7	931.8 ± 6.9	0.01950 ± 0.00044	47 ± 1	1105 ± 25	1001 ± 58	934.5 ± 6.9
OR-B	4.2		1913.3 ± 4.1	9932 ± 200	741.5 ± 2.1	0.2092 ± 0.0005	664 ± 13	13830 ± 41	13745 ± 73	771 ± 2
OR-7	5.7	0.0689	1621.3 ± 3.4	5882 ± 19	992.3 ± 3.0	0.25757 ± 0.00119	1170 ± 6	14916 ± 77	14864 ± 81	1034.8 ± 3.1
OR-6	11.8	0.1408	19.6 ± 0.2	4005 ± 14	108954.5 ± 954.1	15.16264 ± 0.16918	1224 ± 7	15793 ± 235	15741 ± 236	113911.3 ± 1000.4
OR-6R	11.8		1124.7 ± 2.4	5911 ± 119	1146.8 ± 2.5	0.2966 ± 0.0008	931 ± 19	16008 ± 50	15938 ± 70	1200 ± 3
OR-11	26.3	0.1720	378.4 ± 1.0	954 ± 4	1240.0 ± 5.5	0.34451 ± 0.00135	2252 ± 12	17940 ± 89	17908 ± 90	1304.3 ± 5.8
OR-5	36.9	0.1343	1524.0 ± 3.7	6190 ± 101	1337.9 ± 3.6	0.40364 ± 0.00904	1637 ± 45	20286 ± 492	20237 ± 493	1416.7 ± 4.3
OR-4	38.9	0.0932	1456.1 ± 2.8	15513 ± 63	1318.8 ± 3.3	0.37993 ± 0.00254	587 ± 4	19176 ± 141	19046 ± 155	1391.8 ± 3.5
OR-Q	–		843 ± 1.6	54445 ± 1094	1435.5 ± 2.7	0.5106 ± 0.0012	130 ± 3	25074 ± 72	24331 ± 530	1538 ± 4
OR-3	39.3	0.0928	621.9 ± 1.1	33539 ± 143	911.3 ± 3.0	0.60744 ± 0.00501	186 ± 2	40366 ± 399	39587 ± 557	1019.1 ± 3.7
OR-2	42.8	0.0938	2503.3 ± 5.6	6752 ± 19	832.7 ± 2.9	0.58908 ± 0.00219	3598 ± 15	40965 ± 196	40925 ± 197	934.8 ± 3.3
OR-10	45.0	0.1810	233.3 ± 0.7	2989 ± 6	772.8 ± 5.5	0.59350 ± 0.00273	764 ± 3	43082 ± 288	42883 ± 303	872.2 ± 6.3
OR-9	47.1	0.1610	232.0 ± 0.3	2584 ± 5	851.5 ± 3.4	0.61554 ± 0.00211	911 ± 3	42655 ± 198	42490 ± 215	960.0 ± 3.9
OR-1	51.0	0.4172	886.7 ± 1.4	8192 ± 22	901.5 ± 2.5	0.69185 ± 0.00269	1234 ± 5	47434 ± 237	47301 ± 245	1030.4 ± 3.0

Analytical errors are 2σ of the mean. U and Th decay constants are the same as those described in Cheng et al. (2009a, 2009b).

[a] $\delta^{234}U = ([^{234}U/^{238}U]_{activity} - 1) \times 1000$. $\delta^{234}U_{initial}$ (corrected) was calculated based on ^{230}Th age (T), i.e., $\delta^{234}U_{initial} = \delta^{234}U_{measured} \times e^{\lambda 234^* T}$, and T is corrected age.

[b] $[^{230}Th/^{238}U]_{activity} = 1 - e^{-\lambda 230 T} + (\delta^{234}U_{measured}/1000)[\lambda_{230}/(\lambda_{230} - \lambda_{234})](1 - e^{-(\lambda 230 - \lambda 234)T})$, where T is the age.

[c] The degree of detrital ^{230}Th contamination is indicated by the $[^{230}Th/^{232}Th]$ atomic ratio instead of the activity ratio.

[d] Age corrections were calculated using an average crustal $^{230}Th/^{232}Th$ atomic ratio of $4.4 \times 10^{-6} \pm 2.2 \times 10^{-6}$. Those are the values for a material at secular equilibrium, with the crustal $^{232}Th/^{238}U$ value of 3.8. The errors are arbitrarily assumed to be 50%. As Section 3.1 points out and Fig. 13 shows, the corrections for $^{230}Th_{initial}$ are irrelevant to this paper's conclusions.

Where the fabric of Stalagmite Orum-1 is sufficiently domal, rather than coralloidal, to allow measurement of thickness of layers, those measurements indicate that maximum layer thickness is greatest in Period I and less in Periods II and IV (Fig. 10).

4.5. Mineralogy

Stalagmite Orum-1 consists of both aragonite and calcite, with variation between the two polymorphs of $CaCO_3$ vertically within layers, laterally along layers, and more broadly between the different growth periods (Fig. 11). Vertical variation within layers is commonly evident as a sharp base above which aragonite predominates but makes a gradual transition to calcite, above which there is a sharp boundary with the overlying layer. Along layers in coralloidal intervals, aragonite predominates in the protruding coralloids and calcite is common in the recesses, as expected from variation in saturation state along a speleothem surface where coralloids form (Caddeo et al., 2015). At the largest scale, calcite is most abundant in Period I, and aragonite is most abundant in Periods II to IV (Fig. 10).

4.6. Stable isotopes

Values of $\delta^{13}C$ and $\delta^{18}O$ show a strong covariance in Stalagmite Orum-1, both in terms of overall correlation (Fig. 12) and in terms of coinciding local maxima and minima (Fig. 10). Values of both are greatest in Period II, where $\delta^{13}C$ reaches its maximum value of +4.4‰ relative to VPDB and $\delta^{18}O$ reaches its maximum value of −1.3‰ relative to VPDB. $\delta^{18}O$ reaches its minimum value, −7.8‰ relative to VPDB, in Period I.

Relationships between $\delta^{13}C$ and $\delta^{18}O$ before and after 14.6 ka are different in two respects. First, for any given value of $\delta^{18}O$, $\delta^{13}C$ is about 4‰ less in data after 14.6 ka compared to data before 14.6 ka (Fig. 12). Secondly, correlation of $\delta^{13}C$ with $\delta^{18}O$ is stronger after 14.6 ka, as shown by greater values of r^2 (Fig. 12).

The presence of both aragonite and calcite in the stalagmite means that some of the variation of $\delta^{13}C$ and $\delta^{18}O$ along the stalagmite's growth axis results from varying abundance of the two polymorphs. However, the differences between Period I and Period II are >1.7‰ for $\delta^{13}C$ and >0.8‰ for $\delta^{18}O$, and thus greater than the differences that could result simply from change in the polymorph precipitated under

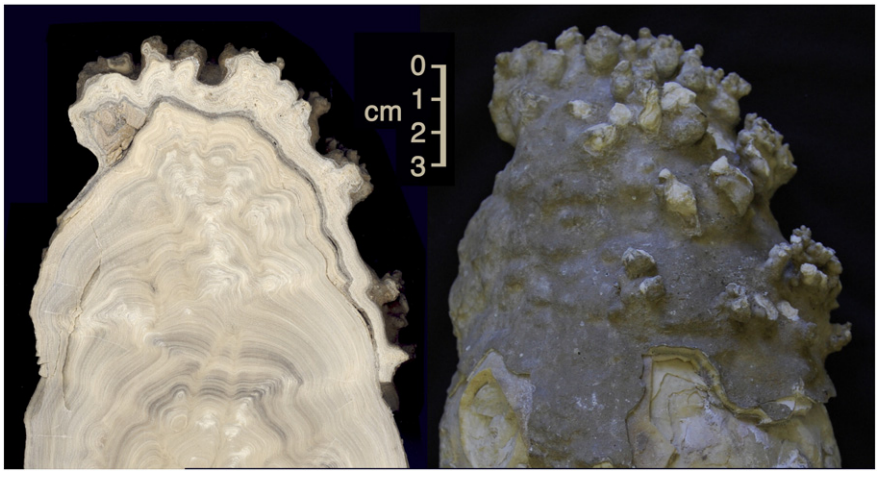

Fig. 6. A. Top of a scanned image of a vertical section of Stalagmite Orum-1. B. Photograph of the exterior of the top of Stalagmite Orum-1 showing protruding coralloids. These coralloids are exposed examples of the structures that dominate much of the interior of Stalagmite Orum-1, as seen in Fig. 4.

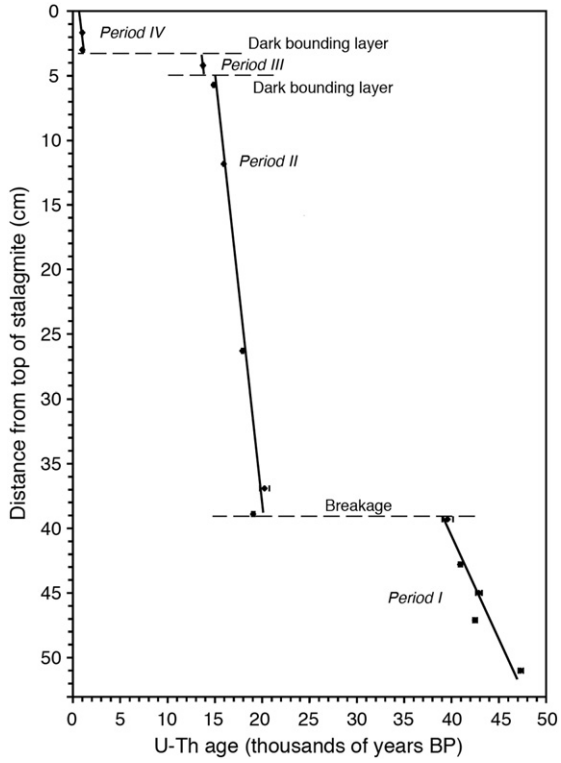

Fig. 7. Age model for Stalagmite Orum-1 discussed in Section 4.2. Regression was used because of the small reversals in age. Growth Period III has only one age because detrital contamination of many laminae allowed drilling of only one sample collectively from multiple laminae throughout the interval.

otherwise identical conditions (Romanek et al., 1992; Kim et al., 2007). The stable isotope data therefore must indicate at least some change of environmental conditions between Period I and Period II, and more generally within and across all of the stalagmite's four periods of growth.

4.7. Summary of results: changes between wetter and drier

Petrography and geochemistry combine in Stalagmite Orum-1 to yield consistent implications with regard to past climate. Across the entire stalagmite, low values of $\delta^{18}O$ coincide with the presence of calcite, with greater thickness of laminae, with more laminated or domal (rather than coralloidal) structure, and with Type E surfaces. Values of $\delta^{18}O$ in stalagmite are controlled by a variety of factors (McDermott, 2004; Lachniet, 2009), but in subtropical regions two important controls are commonly the amount effect and the extent of evaporation (Cuthbert et al., 2014), both of which favor lower $\delta^{18}O$ in wetter conditions.

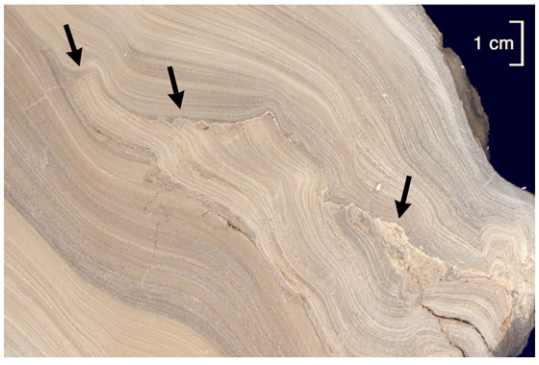

Fig. 8. Surface of breakage (arrows) in Stalagmite Orum-1 that is the boundary between Period I below and Period II above, as discussed in Section 4.2.

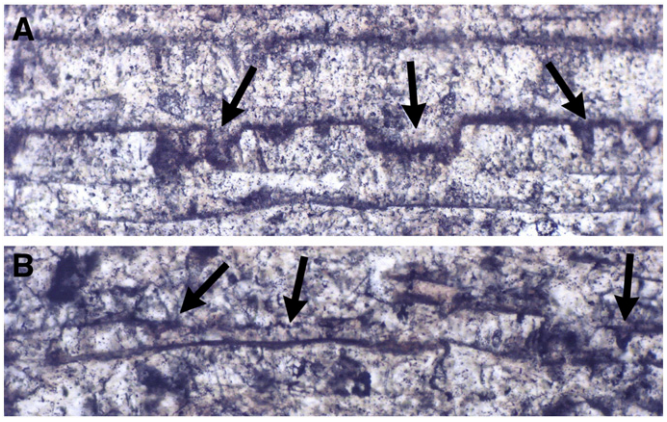

Fig. 9. Photomicrographs of Type E surfaces (arrows) in Stalagmite Orum-1 discussed in Section 4.3. Width of field of view is 2.4 mm in both A and B.

Precipitation of calcite in speleothems is likewise typical of wetter conditions (Murray, 1954; Pobeguin, 1965; Siegel and Dort, 1966; Thrailkill, 1971; Cabrol and Coudray, 1982; Railsback et al., 1994; Frisia et al., 2002). Greater thickness of laminae is similarly suggestive of wetter conditions (Railsback et al., 1994). Greater specific width has also been inferred to reflect wetter conditions (Sletten et al., 2013; Railsback et al., 2014). Laminated or domal structure of a stalagmite is similarly reflective of wetter conditions, because it results from gravity-driven flow rather than capillary movement (Caddeo et al., 2015). Thus all these features combine to suggest wetter conditions. On the other hand, their opposites (greater $\delta^{18}O$, aragonitic mineralogy, lesser thickness of laminae, lesser specific width, and coralloidal structure) all coincide in Stalagmite DP1 and all are suggestive of drier conditions.

In Periods I and II, $\delta^{13}C$ follows the pattern discussed in the previous paragraph, and its variation leads to the same inference. Like values of $\delta^{18}O$, values of $\delta^{13}C$ in stalagmite $CaCO_3$ are controlled by a variety of factors (McDermott, 2004). One of the most important is the input of CO_2 by soil biomass and thus the extent of vegetation (e.g., Hesterberg and Siegenthaler, 1991; Baldini et al., 2005), which in semi-arid environments is commonly dependent on rainfall (as documented in parts of Namibia by Rohde and Hoffman, 2012). After the CO_2 reaches the cave, precipitation of carbonate from the moving dripwater, called "prior calcite precipitation" or more generally "prior carbonate precipitation" (PCP), can lead to degassing of CO_2 and thus an increase in $\delta^{13}C$. PCP is more likely during drier times, because the water's saturation state with respect to either aragonite or calcite is greater and because P_{CO2} of cave air may be less. The relationship of soil biological activity, of degassing, and of PCP to wetness, and thus largely to rainfall, coincide so that greater $\delta^{13}C$ of stalagmite carbonate commonly suggests drier climate, a conclusion also reached by Johnson et al. (2006) and Cross et al. (2015).

In Periods III and IV, the relationship of $\delta^{13}C$ to other parameters, especially $\delta^{18}O$, changes. That change is discussed in Section 5.2.

5. Discussion

5.1. Changes in rainfall over the last 47 kyr, and their relationship to global temperature

5.1.1. Period I (47.5 to ~24 ka)

The consistent patterns in petrography and geochemistry discussed in Section 4.7 suggest major changes in availability of moisture at Orumana over the last 48 kyr. In Period I, which spans much of the last glacial period, low values of $\delta^{18}O$ and $\delta^{13}C$, dominance of calcite, greater width of the stalagmite, and presence of Type E surfaces combine to suggest wet conditions suggestive of more rainfall than at any

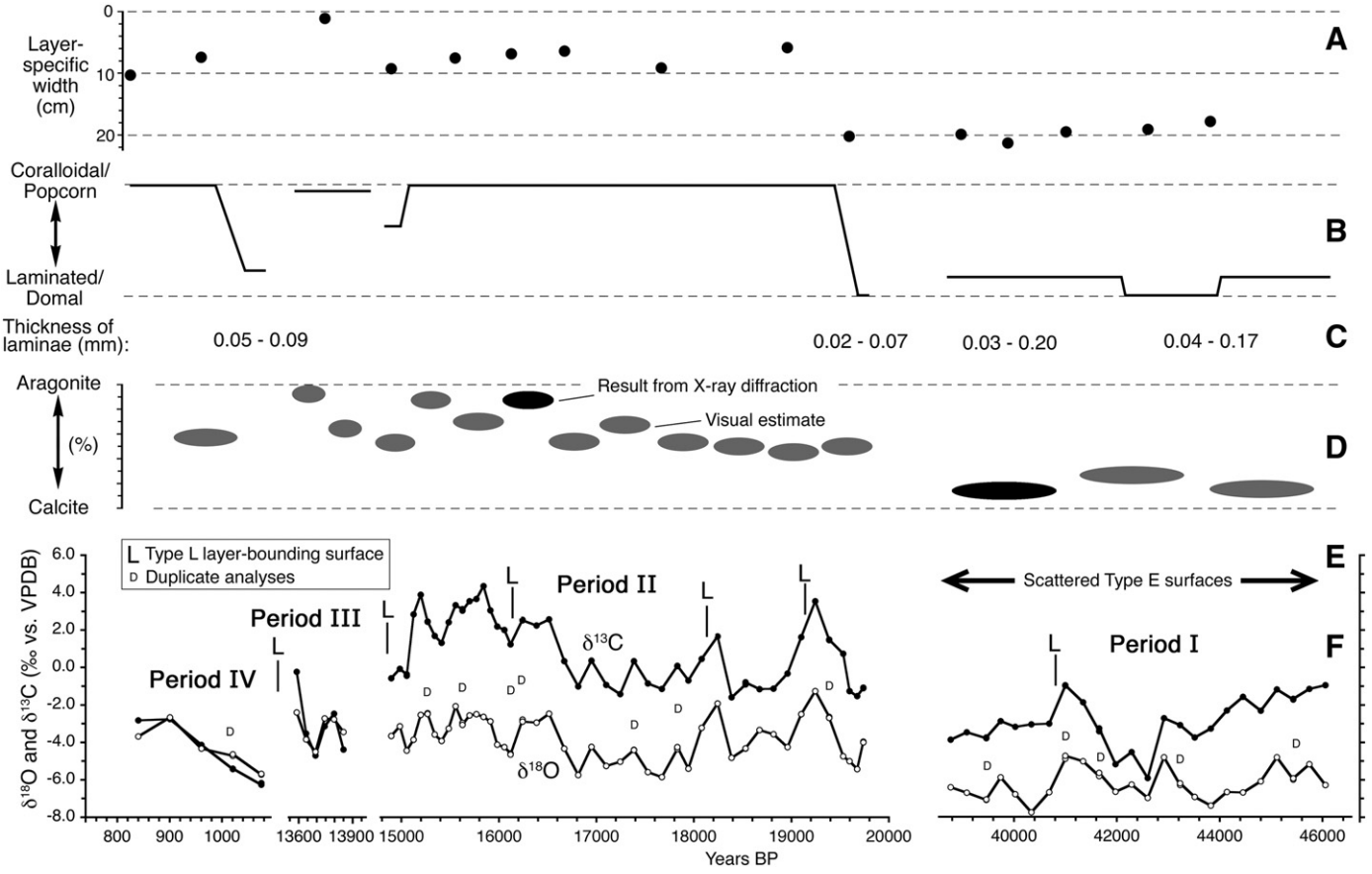

Fig. 10. Plots of petrographic, mineralogical, and isotopic variation along the growth axis of Stalagmite Orum-1. All plots are arranged with indicators of dryness upward and wetness downward. A. Layer-specific width of the stalagmite. B. Shape of the layers of the stalagmite, which range from laminae to coralloids, and form of the stalagmite when these layers were deposited, which correspondingly ranged from domal to popcorn-encrusted. C. Thickness of laminae. In coralloidal intervals, layer thickness is not reported because thickness varies from crest to flanks of individual coralloids and because layers are inclined, so that most observations in thin section are apparent thicknesses that are greater than actual thicknesses. D. Proportions of calcite and aragonite. Observations were made across entire thin sections or parts thereof to give the ovoids shown; X-ray diffraction of powders drilled from two intervals (darker ovoids) allowed quantitative calibration of visual estimates. E. Locations of Type E and Type L surfaces, indicative of exceptionally wet and exceptionally dry conditions, respectively. F. Carbon and oxygen stable isotope data. "D"s indicate duplicate analyses of single samples. Inferences from this figure are summarized in Fig. 13B.

subsequent time in the Orum-1 record (Fig. 10). Period I coincides with the period in which silts were deposited during floods much farther down the Hoarusib drainage (Srivastava et al., 2005), further supporting the notion of conditions during MIS 3 and into MIS 2 wetter than those of today (Fig. 13C). Period I also coincides with the lowest values of δD of n-C_{31}alkane in Core MD08-3167 off the Namibian coast, where lower values indicate wetter conditions (Collins et al., 2014) (Fig. 13F). The regional paleoclimate proxies thus support the notion of wetter climate at Orumana, especially in the period from about 42 to 46 ka.

Period I falls largely within MIS 3 during the last glacial, rather than interglacial, phase of the Pleistocene (Fig. 13). Period I as a whole coincides with the Late Pleistocene low in sea-surface temperature (i.e., normalized SST < −0.8 °C) in the reconstruction by Shakun et al. (2015) (Fig. 13D) and with the low values of $\delta^{18}O$ in the NorthGRIP ice core that prevailed from the beginning of Greenland Stadial 13 (GS-13) to the end of GS-3. The minimum in $\delta^{13}C$ (and local minimum in $\delta^{18}O$) at 41–43 ka in the Orum-1 record coincides with MIS 3b (Railsback et al., 2015), the time of greatest $\delta^{18}O$ within MIS 3 as suggested by the stacked record of $\delta^{18}O$ values from marine benthic foraminifera of Lisiecki and Raymo (2005). All of these observations suggest that the wet conditions at Orumana in Period I were coincident with exceptionally cold global-scale conditions. This conclusion parallels that of Brook et al. (2013) of higher lake levels during the Late Pleistocene (from 34 to 26 ka) than during the Holocene at Etosha Pan, in northern Namibia. It likewise parallels the inference of "mega-lake" phases from 42 to 16 ka in Palaeolake Makgadikgadi in northern Botswana by Burrough and Thomas (2009). It also parallels the conclusion of Lim et al. (2016) of "increased humidity" (compared to the Holocene) "during the last glacial period" based on pollen data from Pella in South Africa, just across the Orange River from southern Namibia.

5.1.2. Period II (20 to 14.5 ka)

The consistent patterns in petrography and geochemistry discussed in Section 4.7 suggest that Period II was a time of decreasing wetness, relative to Period I. Indicators of drying during Period II include increasing $\delta^{18}O$ and $\delta^{13}C$, increasing proportion of aragonite, lesser width of the stalagmite, presence of Type L surfaces, absence of Type E surfaces, and development of coralloids (Fig. 10). Period II coincides with increasing values of δD of n-C_{31} alkane in Core MD08-3167 off the Namibian coast, particularly from 17 to 15 ka, suggesting progressively drier conditions in the region (Collins et al., 2014) (Fig. 13F).

Period II coincides with increasing SST in the global-scale reconstruction by Shakun et al. (2015) (Fig. 13D) and with GS-2, a warmer stadial than previous stadials and one within which warming is evident. More regionally, it coincides with warming in the planktic foram record from Core 64PE-174P13 from the Walvis Ridge, again from 17 to 15 ka (Fig. 13G). These relationships suggest that progressively drier conditions at Orumana in Period II were coincident with progressively warmer global-scale conditions in a transition from the locally wet and globally cold configuration of Period I.

5.1.3. Periods III and IV and their associated hiatuses

Values of $\delta^{18}O$ like those from later in Period II, combined with abundance of aragonite, small layer-specific width of the stalagmite, and the

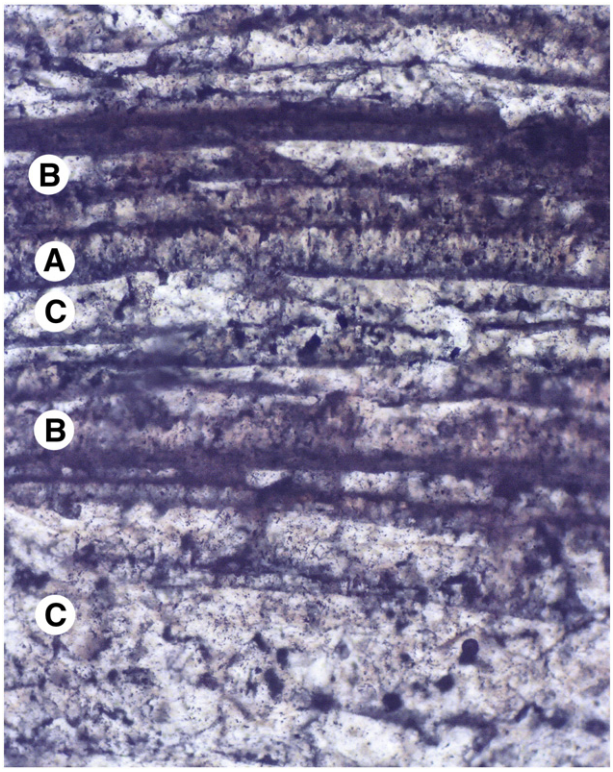

Fig. 11. Photomicrograph of layers of aragonite and calcite in Stalagmite Orum-1. Layers vary from entirely aragonite (A) to both aragonite and calcite (B) to entirely calcite (C), as discussed in Section 4.5. Width of field of view is 2.4 mm.

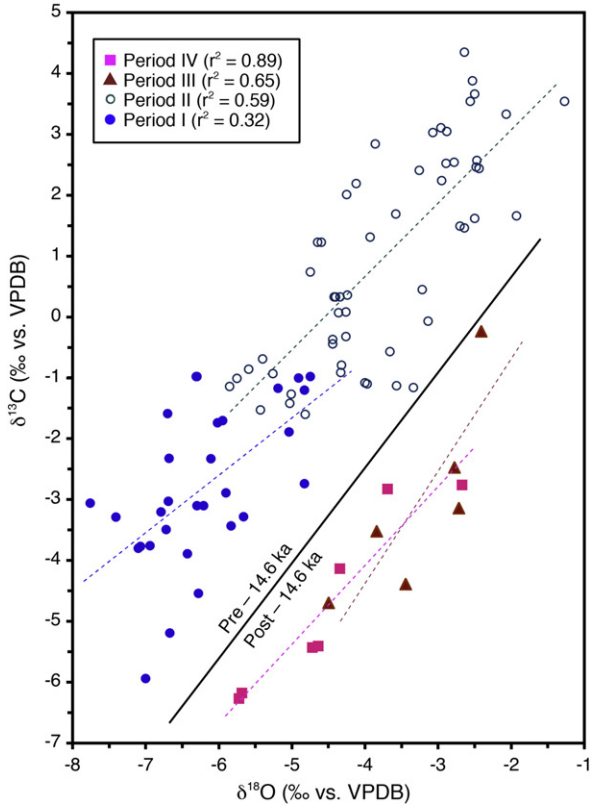

Fig. 12. Plot of carbon and oxygen stable isotope data from Stalagmite Orum-1 discussed in Section 4.6. Solid line emphasizes that data from Periods I and II (earlier) do not overlap with those from Periods III and IV (later). Dashed lines are results of linear regression for data from each of the four time periods. Data are plotted as a time-series in Fig. 10F.

dominance of coralloidal structure, suggest that Periods III (late in Termination I) and IV (in the late Holocene) were as dry as those late in Period II (and the shift in vegetation inferred in Section 5.2 suggests that they may have actually been drier). Periods III and IV coincide with the greatest values of δD of *n*-C_{31}alkane in Core MD08-3167 off the Namibian coast, suggesting dry conditions in the region. (Collins et al., 2014) (Fig. 13F). The three hiatuses between Periods II and III (during the Bølling-Allerød), between Periods III and IV (during the early to middle Holocene), and after Period IV (the last 800 years) by definition leave no direct evidence of environmental conditions, but the absence of Type E surfaces atop coralloids suggests that deposition stopped because of exceptional dry, rather than exceptionally wet, conditions. This conclusion of dry conditions in the Holocene parallels the finding of "increased aridity" in the Holocene relative to glacial times inferred from palynological evidence from Pella in South Africa across the Orange River from southern Namibia (Lim et al., 2016). Dry conditions during the present as well as previous interglacial are also supported by abundances of luminescence ages from the Namib Sand Sea (Stone et al., 2015, Table 1). However, in detail the results from Stalagmite Orum-1 are not in accord with the findings of Chase et al. (2009, 2010) of wettest Holocene conditions in the early to middle Holocene from studies of hyrax middens in western Namibia.

Periods III and IV coincide with post-glacial conditions at the beginning and end of MIS 1. The hiatus between Periods II and III coincides with the Bølling-Allerød or Greenland Interstadial 1 (GI-1), which both the NorthGRIP (Greenland) and EPICA Dome C (Antarctic) records suggest was warmer than any interstadial over the previous 60 kyr. The much longer hiatus between Periods III and IV coincides with the even warmer early to middle Holocene, the altithermal. The overall pattern that emerges is thus a spelean record of wetter climate at Orumana in coldest (fully glacial) global conditions, a spelean record of progressively drier climate with post-glacial warming, and hiatuses suggestive of driest conditions during the warmest periods of global climate.

5.2. A change in vegetation after 14.6 ka

The change in isotope systematics after 14.6 ka (Fig. 12) suggests a change in vegetation at Orumana from the C_4-rich savanna ecosystem presently east of Orumana to the semidesert ecosystem at Orumana today. Values of $\delta^{18}O$ from Periods III and IV, after 14.6 ka, are neither as low as the lowest values of Period I nor as high as the highest values in Period II; in short, they are not exceptional. However, two differences in the relationship between $\delta^{13}C$ and $\delta^{18}O$ before and after 14.6 ka suggest changes in the nature and dynamics of the vegetation. First, for any given value of $\delta^{18}O$, $\delta^{13}C$ is about 4‰ less in data after 14.6 ka compared to data before 14.6 ka (Fig. 12). This change can be explained by a change from vegetation with a large component of C_4 vegetation to one with fewer C_4 plants. Secondly, the correlation of $\delta^{13}C$ with $\delta^{18}O$ is stronger after 14.6 ka, as shown by greater values of r^2 (Fig. 12). This change can be explained by a transition to an ecosystem in which the extent of vegetation was more directly responsive to temporal changes in rainfall, presumably in drier conditions.

These changes would suggest that the modern wetter region of C_4-rich savanna east and north of Orumana (Fig. 3) extended farther southwest prior to 14.6 ka, encompassing the area at Orumana. After 14.6 ka, with Holocene warming, that savanna ecosystem seems to have retreated to its present range, leaving Orumana and perhaps more land to the south and west in the modern dry and grass-poor semidesert ecosystem seen today. This inference agrees with the results of Collins et al. (2014), who found a major shift in $\delta^{13}C$ of *n*-C_{31}alkane from 19 to 11 ka in Core MD08-3167 off the Namibian coast (Fig. 13E), and who inferred a change from C_4 to C_3 vegetation as summer rainfall decreased.

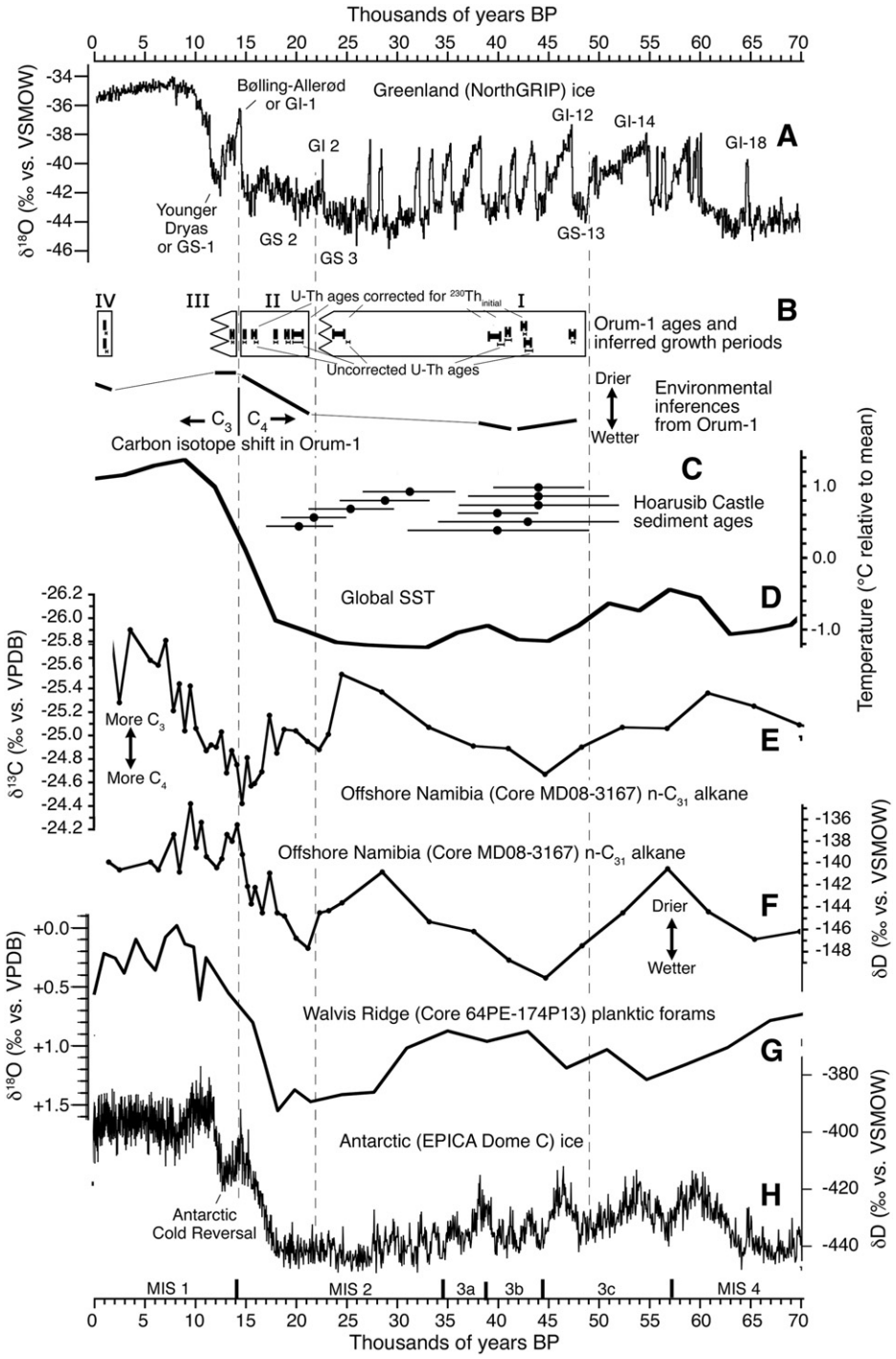

Fig. 13. Paleoclimate records, from north to south. A. Oxygen isotope record from the NorthGRIP core in Greenland (North Greenland Ice Core Project Members, 2007). GS (Greenland Stadial) and GI (Greenland Interstadial) designations follow the INTIMATE conventions of Björck et al. (1998) and Mogensen (2009). B. Ages and growth periods of Stalagmite Orum-1, and a summary of inferences about past climate from Fig. 10 (this study). Zigzags indicate age limits for growth periods made indefinite by breakage of the stalagmite. The carbon isotope shift marked is the shift discussed in Section 5.2. C. OSL ages of flood-generated sediments in the Hoarusib catchment from Srivastava et al. (2005). D. Sea-surface temperature anomalies from Shakun et al. (2015). E and F. Stable isotope data from leaf wax in a marine core off the coast of Namibia (Collins et al., 2014). Arrows indicate inferences about vegetation and climate and are taken from Fig. 3 of Collins et al. (2014). G. Oxygen isotope record from planktonic foraminifera from Core 64PE-17P13 of Scussolini and Peeters (2013). Locations of cores for E, F, and G are shown in Fig. 1. H. Hydrogen isotope data from the EPICA Dome C ice core (Jouzel et al., 2007) plotted using the chronology of Bazin et al. (2013). Marine isotope stages (MIS) and substages are from Railsback et al. (2015).

5.3. Climate change from the Last Glacial Maximum to the Holocene

5.3.1. General models

Great diversity of opinion exists in comparing the climate of southwestern Africa during the Last Glacial Maximum (LGM) to that of the Holocene and today. At one extreme is the view that climate during the LGM was drier than that of today (Partridge et al., 1999; Tyson et al., 2001), which is supported by records on land (Eitel et al., 2006) and by data from marine cores (Dupont and Wyputta, 2003). This view of an LGM drier than today is further supported by U-Th ages of

speleothems indicating deposition only in the interglacials, rather than in glacial stages, that preceded the LGM (Geyh and Heine, 2014). At the other extreme is the view that climate was wetter during glacial times than in the Holocene, with support from records on land (Thomas et al., 2003; Srivastava et al., 2005; Schefuß et al., 2011) and from marine cores (Stuut et al., 2002; Collins et al., 2014). Evidence for this view is especially strong in the Khumib and Hoarusib river valleys in northernmost Namibia, as shown in Fig. 4A of Stone and Thomas (2013).

This dichotomy of interpretations is paralleled by, and in some cases underlain by, a dichotomy of models of climate change. In the earlier model, cooling of global climate (e.g., during the LGM) results in expansion of the cold polar region dominated by Antarctica ("an expansion of the circumpolar vortex" in the words of Partridge et al., 1999). As a result, northward shifts of climate belts move the summer rainfall region northward and thus leave much of southern Africa drier (Cockroft et al., 1987; Partridge et al., 1999). In the later model, cooling of global climate is most intense in the Northern Hemisphere because of the great land area of that hemisphere, especially across Eurasia. As a result, the Intertropical Convergence Zone (ITCZ) moves toward the warmer southern hemisphere (Kang et al., 2008), with resultant southward shifts of climate belts that move the summer rainfall region southward and thus leave much of southern Africa wetter. Southward migration of the ITCZ with cooling of the Northern Hemisphere, and conversely northward migration with warming of the Northern Hemisphere, has been suggested by paleoclimatalogical research (Koutavas and Lynch-Stieglitz, 2004; Russell and Johnson, 2005; Brown and Johnson, 2005; Sinha et al., 2011; Leech et al., 2013), supported by several modeling studies (Chiang et al., 2003; Broccoli et al., 2006; Kang et al., 2008; Frierson and Hwang, 2012; McGee et al., 2014), and endorsed by thorough reviews (Chiang and Friedman, 2012; Schneider et al., 2014). Most significantly with regard to southern Africa, Schefuß et al. (2011) concluded that southward migration of the ITCZ in response to cooling in the Northern Hemisphere led to greater rainfall in southeastern Africa at least twice in the last 17 kyr.

A third general view might be that the geography of climatic and ecological zones in southwestern Africa is sufficiently complex, with changes from north to south and from coast to inland (Figs. 1–3), that no simple model will account for past climate change, as suggested by Singarayer and Burrough (2014). This means that multiple boundaries may change in different directions as global climate changes, and that marine records of continental climate face the challenge of mixing from multiple sources sending different signals. Additionally, the region has two potential sources of water vapor, the Indian and Atlantic (as pointed out by Collins et al., 2014), with the Atlantic contribution made variable by changes in the Angola-Benguela Front (ABF) (Veitch, 2002; Rouault et al., 2003) and the Inter-Ocean Convergence Zone (IOCZ/CAB) (Tyson, 1986; Mattes and Mason, 1998). Thus the most sound conclusion of this section's review of general models of past climate in southwestern Africa is that no one simple model will explain past climate in all locations.

5.3.2. Past climate at Orumana in the larger African context

The linkage of locally wetter conditions to globally cooler climate inferred from the Orum-1 record in Section 5.1 suggests that the best understanding of past climate at Orumana may lie in a synthesis of the global-scale model of movement of the ITCZ (the second model in Section 5.3.1) with recognition of the complexity of climate in southern Africa (the third view in Section 5.3.1). One important observation in applying the global-scale ITCZ model is that the ITCZ has a complex configuration across Africa. In Africa west of about 13°E longitude (which is highlighted on Fig. 2), the ITCZ lies north of the equator year-round (Fig. 2), with the northern bias typical around the globe and especially over the oceans (e.g., Fig. 1 of Wang, 2009). East of 13°E in Africa, the summer and winter positions of the ITCZ are almost symmetrical north and south of the equator (Fig. 2), a configuration unusual in the modern world (and one exceeded in southern bias only by the ITCZ's similar configuration in eastern South America). Thus one observation in comparing the modern configuration of the ITCZ to possible past configurations is that the ITCZ east of 13°E presently has a comparative bias to the south that might be unlikely to increase with a global shift of the ITCZ southward, but the ITCZ west about 13°E in Africa and the eastern Atlantic presently has a strong regional bias to the north that would allow a significant movement to the south during a global shift of the ITCZ southward.

A second important observation, not relevant to all of Africa but critical to northwestern Namibia and southern Angola, is that the Angola-Benguela Front (ABF) at sea matches in latitude a major environmental shift on land. At the latitude of the ABF, the Namib Desert dominating the coast to the south reaches its northern boundary, and rainfall farther inland increases abruptly from south to north, from <600 mm/yr to >1000 mm/yr (Fig. 2). The fact that southward penetration of the Angola Current is known to increase rainfall inland (Rouault et al., 2003) suggests that the latitudinal match of the ABF with the marked change in wetness on land represents a causal relationship in which the Angola Current contributes to the wetness of climate in south-central Angola, just north and east of Orumana.

A third important observation is that the Inter-Ocean Convergence Zone (IOCZ) or Congo Air Boundary (CAB) is a zone of enhanced rainfall that, in present climatology, lies just north of Orumana during austral summer (Fig. 2). Any southward shift of the summer IOCZ or CAB would presumably bring more rainfall to northern Namibia.

These three observations combine to suggest that a general shift of the ITCZ southward during the LGM (Chiang et al., 2003; Koutavas and Lynch-Stieglitz, 2004; Leech et al., 2013; Schneider et al., 2014), significant west of 13°E while perhaps insignificant east of that line, could have induced a southward shift of the ABF and/or IOCZ that led to increased rainfall in northern Namibia. Arbuszewski et al. (2013) estimated that the ITCZ in the Atlantic Ocean shifted southward about seven degrees of latitude during the LGM. Like the ITCZ, the ABF shifts northward in winter and southward in summer (Fig. 2), suggesting that the ABF would have shifted southward with a long-term southward shift of the ITCZ during the LGM. The IOCZ or CAB likewise shifts northward in winter and southward in summer (Fig. SD.3 of van Heerden and Taljaard (1998)), suggesting a possible long-term shift southward of the IOCZ or CAB concomitantly with a long-term southward shift of the ITCZ during the LGM. Any southward shift of the IOCZ or CAB and/or ABF would presumably have been smaller than that of the ITCZ reported by Arbuszewski et al. (2013) for the LGM, but present patterns of rainfall suggest that a southward shift of only three degrees of latitude would lead to a doubling of rainfall at Orumana (Fig. 2).

This explanation of the Stalagmite Orum-1 record of wetter glacial times at Orumana may explain how northern Namibia was wet when southern Namibia seemingly remained dry in the LGM. The results from Orum-1 are in accord with the OSL ages of Srivastava et al. (2005) for the Hoarusib Clay Castles flood sediments in suggesting that at least the Hoarusib catchment was wetter during glacial times. However, results from farther south, perhaps most notably the interglacial but not glacial ages of speleothems at 22.5°S reported by Geyh and Heine (2014), suggest that the wetness during glacial times at Orumana did not extend far to the south, and thus that any southward shift of the ABF and/or IOCZ, and of the rainfall typical of modern southern Angola, may have been limited latitudinally. A southward shift of the ABF and/or IOCZ in western southern Africa, but not in eastern southern Africa, may explain why some results from the latter region (e.g., those of Truc et al. (2013) from Wonderkrater at 29°E) support neither a wetter LGM there nor southward migration of the (eastern African) ITCZ. A climate dipole between western and eastern southern Africa (Woodborne et al., 2015) may additionally make the climate record of east southern Africa unlike that of the west.

6. Conclusions

Several different kinds of data (carbon and oxygen stable isotopes, mineralogy, petrographic fabrics, layer-bounding surfaces, layer-specific width, and layer thickness) from Stalagmite Orum-1 combine with 13 U-Th ages to suggest major changes in climate in northeastern Namibia over the last 47 kyr. Specifically, climate was wetter in northwestern Namibia during glacially cold MIS 3 than it is today, and grass densities were greater. During the deglacial period after the LGM, the climate at Orumana became drier, but C_4 grasses persisted. In the Holocene, seemingly still drier conditions led to loss of those grasses and to a semi-desert biome. The Bølling-Allerød (GI-1) and early Holocene are represented by hiatuses suggesting even drier conditions. Thus the general pattern is wetter climate at Orumana in coldest (fully glacial) global conditions, progressively drier climate with post-glacial warming, and hiatuses suggestive of driest conditions during the warmest periods of global climate. That pattern suggests a southward shift of the ITCZ over the eastern South Atlantic and western Africa during glacial times, leading to a lesser but correlative southward shift of the ABF and/or IOCZ to bring wetter conditions to northern Namibia. Warmer global conditions conversely seem to have involved a shift of the ITCZ, ABF, and/or IOCZ northward to give dry climate in northern Namibia. If so, then extrapolation to warmer conditions in the next century, with a further northward shift of the ITCZ and thus the ABF and/or IOCZ, would suggest further drying in at least northern Namibia and southern Angola.

Acknowledgments

This research was carried out with permissions from the Namibia National Monuments Council and Ministry of Environment & Tourism; it was funded by National Science Foundation grant 0725090 to Brook. Jaco and Ciska Olivier assisted in collecting the stalagmite.

References

Arbuszewski, J.A., deMenocal, P.B., Cléroux, C., Bradtmiller, L., Mix, A., 2013. Meridional shifts of the Atlantic intertropical convergence zone since the Last Glacial Maximum. Nat. Geosci. 6, 959–962.

Atlas of Namibia Project, 2002. Grass cover in Namibia (map, 1:7,500,000). Directorate of Environmental Affairs, Namibia Ministry of Environment and Tourism, as provided by the Digital Atlas of Namibia hosted by the University of Cologne (www.uni-koeln.de/sfb389/e/e1/download/atlas_namibia/index_e.htm).

Baldini, J.U.L., McDermott, F., Baker, A., Baldini, L.M., Mattey, D.P., Railsback, L.B., 2005. Biomass effects on stalagmite growth and isotope ratios: a 20th century analogue from Wiltshire, England. Earth Planet. Sci. Lett. 240, 486–494.

Bazin, L., Landais, A., Lemieux-Dudon, B., Kele, H.T.M., Veres, D., Parrenin, F., Martinerie, P., Ritz, C., Capron, E., Lipenkov, V., Loutre, M.F., Raynaud, D., Vinther, B., Svensson, A., Rasmussen, S.O., Severi, M., Blunier, T., Leuenberger, M., Fischer, H., Masson-Delmotte, V., Chappellaz, J., Wolff, E., 2013. An optimized multi-proxy, multi-site Antarctic ice and gas orbital chronology (AICC2012): 120-800 ka. Clim. Past 9, 1715–1731.

Benthien, A., Andersen, N., Schulte, S., Müller, P.J., Schneider, R.R., Wefer, G., 2005. The carbon isotopic record of the $C_{37:2}$ alkenone in the South Atlantic: Last Glacial Maximum (LGM) vs. Holocene. Palaeogeogr. Palaeoclimatol. Palaeoecol. 221, 123–140.

Björck, S., Walker, M.J.C., Cwynar, L.C., Johnsen, S., Knudsen, K.-L., Lowe, J.J., Wohlfarth, B., intimate members, 1998. An event stratigraphy for the Last Termination in the North Atlantic region based on the Greenland ice-core record: a proposal by the INTIMATE group. J. Quat. Sci. 13 (4), 283–292.

Broccoli, A.J., Dahl, K.A., Stouffer, R.J., 2006. Response of the ITCZ to Northern Hemisphere cooling. Geophys. Res. Lett. 33, L01702. http://dx.doi.org/10.1029/2005GL024546.

Brook, G.A., Railsback, L.B., Marais, E., 2011. Reassessment of carbonate ages by dating both carbonate and organic material from an Etosha Pan (Namibia) stromatolite: evidence of humid phases during the last 20 ka. Quat. Int. 229, 24–37.

Brook, G.A., Cherkinsky, A., Railsback, L.B., Marais, E., Hipondoka, M.H.T., 2013. ^{14}C dating of organic residue and carbonate from stromatolites in Etosha Pan, Namibia: ^{14}C reservoir effect, correction of published carbonate ages, and evidence of >8 m deep lake during the Late Pleistocene. Radiocarbon 55, 1156–1163.

Brown, E.T., Johnson, T.C., 2005. Coherence between tropical East African and South American records of the Little Ice Age. Geochem. Geophys. Geosyst. 6, Q12005. http://dx.doi.org/10.1029/2005GC000959.

Burrough, S.L., Thomas, D.S.G., Bailey, 2009. Mega-Lake in the Kalahari: a Late Pleistocene record of the Palaeolake Makgadikgadi system. Quat. Sci. Rev. 28, 1392–1411.

Cabrol, P., Coudray, J., 1982. Climatic fluctuations influence the genesis and diagenesis of carbonate speleothems in southwestern France. Natl Speleol. Soc. Bull. 44, 112–117.

Caddeo, G.A., Railsback, L.B., De Waele, J., Frau, F., 2015. Stable isotope data as constraints on models for the origin of coralloid and massive speleothems: the interplay of substrate, water supply, degassing, and evaporation. Sediment. Geol. 318, 130–141.

Chase, B.M., Meadows, M.E., Scott, L., Thomas, D.S.G., Marais, E., Sealy, J., Reimer, P.J., 2009. A record of rapid Holocene climate change preserved in hyrax middens from southwestern Africa. Geology 37, 703–706.

Chase, B.M., Meadows, M.E., Carr, A.S., Reimer, P.J., 2010. Evidence for progressive Holocene aridification in southern Africa recorded in Namibian hyrax middens: implications for African Monsoon dynamics and the "African Humid Period". Quat. Res. 74, 36–45.

Cheng, H., Edwards, R.L., Hoff, J., Gallup, C.D., Richards, D.A., Asmerom, Y., 2000. The half-lives of uranium-234 and thorium-230. Chem. Geol. 169 (1–2), 17–33.

Cheng, H., Fleitmann, D., Edwards, R.L., Wang, X.F., Cruz, F.W., Auler, A.S., Mangini, A., Wang, Y.J., Burns, S.J., Matter, A., 2009a. Timing and structure of the 8.2 ky event inferred from $\delta^{18}O$ records of stalagmites from China, Oman and Brazil. Geology 37, 1007–1010.

Cheng, H., Edwards, R.L., Broecker, W.S., Denton, G.H., Kong, X.G., Wang, Y.J., Zhang, R., Wang, X.F., 2009b. Ice Age terminations. Science 326, 248–252.

Chiang, J.C.H., Friedman, A.R., 2012. Extratropical cooling, interhemispheric thermal gradients, and tropical climate change. Annu. Rev. Earth Planet. Sci. 40, 383–412.

Chiang, J.C.H., Biasutti, M., Battisti, D.S., 2003. Sensitivity of the Atlantic Intertropical Convergence Zone to Last Glacial Maximum boundary conditions. Paleoceanography 18. http://dx.doi.org/10.1029/2003PA000916.

Chi-Bonnardel, R.V., 1973. Atlas of Africa. Institut Geographique National (France). Editions Jeune Afrique, Paris (335 p.).

Cockroft, M.J., Wikinson, M.J., Tyson, P.D., 1987. The application of a present-day climate model to the Late Quaternary in southern Africa. Clim. Chang. 10, 161–181.

Collins, J.A., Schfuß, E., Govin, A., Mulitza, S., Tiedemann, R., 2014. Insolation and glacial–interglacial control on southwestern African hydroclimate over the past 140000 years. Earth Planet. Sci. Lett. 398, 1–10.

Craven, P., 2009. Phytogeographic study of the Kaokoveld Centre of Endemism (Unpublished thesis) Stellenbosch University (233 pp.).

Cross, M., McGee, D., Broecker, W.S., Quade, J., Shakun, J.D., Cheng, H., Lu, Y., Edwards, R.L., 2015. Great Basin hydrology, paleoclimate, and connections with the North Atlantic: a speleothem stable isotope and trace element record from Lehman Caves, NV. Quat. Sci. Rev. 127, 186–198.

Cuthbert, M.O., Baker, A., Jex, C.N., Graham, P.W., Treble, P.C., Andersen, M.S., Acworth, R.I., 2014. Drip water isotopes in semi-arid karst: implications for speleothem paleoclimatology. Earth Planet. Sci. Lett. 395, 194–204.

DARA and the Climate Vulnerability Forum, 2010. Climate Vulnerability Monitor 2010: The State of the Climate Crisis. Fundación DARA Internacional, Madrid (290 pp. http://daraint.org/climate-vulnerability-monitor/climate-vulnerability-monitor-2010/download-the-report/).

Dupont, L.M., Wyputta, U., 2003. Reconstructing pathways of aeolian pollen transport to the marine sediments along the coastline of SW Africa. Quat. Sci. Rev. 22, 157–174.

Dupont, L.M., Behling, H., Kim, J.-H., 2008. Thirty thousand years of vegetation development and climate change in Angola (Ocean Drilling Program Site 1078). Clim. Past 4, 107–124.

Edwards, R.L., Chen, J.H., Wasserburg, G.J., 1987. U-238-U-234-TH-230-TH-232 systematics and the precise measurement of time over the past 500,000 years. Earth Planet. Sci. Lett. 81 (2–3), 175–192.

Ehleringer, J.R., 2005. The influence of atmospheric CO_2, temperature, and water on the abundance of C_3/C_4 taxa. In: Ehleringer, J.R., Cerling, T.E., Dearing, M.D. (Eds.), A History of Atmospheric CO_2 and Its Effects on Plants, Animals, and Ecosystems. Ecological Studies vol. 177, pp. 214–231.

Eitel, B., Kadereit, A., Blümel, W.-D., Hüser, K., Lomax, J., Hilgers, A., 2006. Environmental changes at the eastern Namib Desert margin before and after the Last Glacial Maximum: new evidence from fluvial deposits in the upper Hoanib River catchment, northwestern Namibia. Palaeogeogr. Palaeoclimatol. Palaeoecol. 234, 201–222.

Frierson, D.M.W., Hwang, Y.-T., 2012. Extratropical influence on ITCZ shifts in slab ocean simulations of global warming. J. Clim. 25, 720–733. http://dx.doi.org/10.1175/JCLI-D-11-00116.1.

Frisia, S., Borsato, A., Fairchild, I.J., McDermott, F., Selmo, E.M., 2002. Aragonite–calcite relationships in speleothems (Grotte de Clamouse, France): environment, fabrics, and carbonate geochemistry. J. Sediment. Res. 72, 687–699.

Geyh, M.A., Heine, K., 2014. Several distinct wet periods since 420 ka in the Namib Desert inferred from U-series dates of speleothems. Quat. Res. 81, 381–391.

Heine, K., Rust, R., Hilgers, A., 2014. Why 'Younger Dryas'? Why not "Antarctic Cold Reversal'? Eksteenfontein revisited. In: Runge, J. (Ed.), New Studies on Former and Recent Landscape Changes in Africa. Palaeoecology of Africa vol. 32, pp. 163–183.

Hesterberg, R., Siegenthaler, U., 1991. Production and stable isotope composition of CO_2 in a soil near Bern. Switzerland. Tellus 43B, 197–205.

Hill, C., Forti, P., 1997. Cave Minerals of the World. National Speleological Society, Huntsville, Alabama, U.S.A. (238 p.).

Hoffman, P.F., Kaufman, A.J., Halverson, G.P., 1998. Comings and goings of global glaciations in a Neoproterozoic tropical platform in Namibia 8. GSA Today, pp. 1–9.

Hoffmann, K.-H., Prave, A.R., 1996. A preliminary note on a revised subdivision and regional correlation of the Otavi Group based on glaciogenic diamictites and associated cap dolostones. Geol. Surv. Namibia Commun. 11, 77–82.

Irish, J., Marais, E., Juberthie, C., Decu, V., 2001. Namibia. Encycl. Biospeol. 1639–1650.

Johnson, K.R., Hu, C., Belshaw, N.S., Henderson, G.M., 2006. Seasonal trace-element and stable-isotope variations in a Chinese speleothem: the potential for high-resolution paleomonsoon reconstruction. Earth Planet. Sci. Lett. 244, 394–407.

Jouzel, J., Masson-Delmotte, V., Cattani, O., Dreyfus, G., Falourd, S., Hoffmann, G., Minster, B., Nouet, J., Barnola, J.M., Chappellaz, J., Fischer, H., Gallet, J.C., Johnsen, S., Leuenberger, M., Loulergue, L., Luethi, D., Oerter, H., Parrenin, F., Raisbeck, G.,

Raynaud, D., Schilt, A., Schwander, J., Selmo, E., Souchez, R., Spahni, R., Stauffer, B., Steffensen, J.P., Stenni, B., Stocker, T.F., Tison, J.L., Werner, M., Wolff, E.W., 2007. Orbital and millennial Antarctic climate variability over the past 800,000 years. Science 317, 793–796.
Kang, S.M., Held, I.M., Frierson, D.M.W., Zhao, M., 2008. The response of the ITCZ to extratropical thermal forcing: idealized slab-ocean experiments with a GCM. J. Clim. 21, 3521–3532.
Kim, S.T., O'Neil, J.R., Hillaire-Marcel, C., Mucci, A., 2007. Oxygen isotope fractionation between synthetic aragonite and water: influence of temperature and Mg^{2+} concentration. Geochim. Cosmochim. Acta 71, 4704–4715.
Kottek, M., Grieser, J., Beck, C., Rudolf, B., Rubel, F., 2006. World map of the Köppen-Geiger climate classification updated. Meteorol. Z. 15, 259–263.
Koutavas, A., Lynch-Stieglitz, J., 2004. Variability of the marine ITCZ over the eastern Pacific during the past 30,000 years: regional perspective and global context. In: Diaz, H.F., Bradley, R.S. (Eds.), The Hadley Circulation: Present, Past, and Future. Springer, pp. 347–369.
Lachniet, M.S., 2009. Climate and environmental controls on speleothem oxygen-isotope values. Quat. Sci. Rev. 28, 412–432.
Lange, G.-M., 1997. An Approach to Sustainable Water Management Using Natural Resource Accounts: the Use of Water, the Economic Value of Water, and Implications for Policy. Directorate of Environmental Affairs, Namibia Ministry of Environment and Tourism. Res. Discus. Pap. 18.
Leech, P.J., Lynch-Stieglitz, J., Zhang, R., 2013. Western Pacific thermocline structure and the Pacific marine Intertropical Convergence Zone during the Last Glacial Maximum. Earth Planet. Sci. Lett. 363, 133–143.
Lim, S., Chase, B.M., Chevalier, M., Reimer, P.J., 2016. 50,000-years of vegetation and climate change in the southern Namib Desert, Pella, South Africa. Palaeogeogr. Palaeoclimatol. Palaeoecol. 451, 197–209.
Lisiecki, L.E., Raymo, M.E., 2005. A Pliocene-Pleistocene stack of 57 globally distributed benthic $\delta^{18}O$ records. Paleoceanography 20. http://dx.doi.org/10.1029/2004PA001071.
Martini, J.E.J., Marais, J.C.E., Irish, J., 1990. Kaokoveld karst, Namibia. The 1990 SWAKNO Kaokoveld speleological expedition. Bull. S. Afr. Speleol. Assoc. 31, 25–41.
Martini, J.E.J., Marais, J.C.E., Irish, J., 1999. Contribution à l'étude du karst et des grottes du Kaokoland (Namibie). Karstologia 34, 1–8.
Mattes, M., Mason, S.J., 1998. Evaluation of a seasonal forecasting procedure for Namibian rainfall. S. Afr. J. Sci. 94, 183–185.
McCrea, J.M., 1950. On the isotopic chemistry of carbonates and a paleotemperature scale. J. Chem. Phys. 18, 849–857.
McDermott, F., 2004. Palaeo-climate reconstruction from stable isotope variations in speleothems: a review. Quat. Sci. Rev. 23, 901–918.
McGee, D., Donohoe, A., Marshall, J., Ferreira, D., 2014. Changes in ITCZ location and cross-equatorial heat transport at the Last Glacial Maximum, Heinrich Stadial 1, and the mid-Holocene. Earth Planet. Sci. Lett. 390, 69–79.
Mendelsohn, J., Jarvis, A., Roberts, C., Robertson, T., 2002. Atlas of Namibia. David Philip Publishers, Cape Town (200 pp.).
Miller, R.M.G., 2008. The Geology of Namibia. Neoproterozoic to Lower Palaeozoic Vol. 2. Geological Survey of Namibia, Windhoek.
Mogensen, I.A., 2009. Dansgaard-Oeschger cycles. In: Gornitz, V. (Ed.), Encyclopedia of Paleoclimatology and Ancient Environments. Springer, Dordrecht, pp. 229–233.
Murray, J.W., 1954. The deposition of calcite and aragonite in caves. J. Geol. 62, 481–492.
New, M., Hulme, M., Jones, P., 1999. Representing twentieth-century space–time climate variability. Part I: development of a 1961–90 mean monthly terrestrial climatology. J. Clim. 12, 829–856.
Nicholson, S.E., 2009. A revised picture of the structure of the "monsoon" and land ITCZ over West Africa. Clim. Dyn. 32, 1155–1171.
North Greenland Ice Core Project Members, 2007. 50 year means of oxygen isotope data from ice core NGRIP. http://dx.doi.org/10.1594/PANGAEA.586886.
Partridge, T.C., Scott, L., Hamilton, J.E., 1999. Synthetic reconstructions of southern African environments during the Last Glacial Maximum (2–18 kyr) and the Holocene Altithermal (8–6 kyr). Quat. Int. 57 (58), 207–214.
Pobeguin, T., 1965. Sur les concretions calcaires Observées dans la Grotte de Moulis (Ariège). Soc. Geol. Fr., C. R. 241, 1791–1793.
Railsback, L.B., Brook, G.A., Chen, J., Kalin, R., Fleischer, C.J., 1994. Environmental controls on the petrology of a Late Holocene speleothem from Botswana with annual layers of aragonite and calcite. J. Sediment. Res. A64, 147–155.
Railsback, L.B., Akers, P.D., Wang, L., Holdridge, G.A., Voarintsoa, N., 2013. Layer-bounding surfaces in stalagmites as keys to better paleoclimatological histories and chronologies. Int. J. Speleol. 42, 167–180.
Railsback, L.B., Xiao, H., Liang, F., Akers, P.D., Brook, G.A., Dennis, W.M., Lanier, T.E., Cheng, H., Edwards, R.L., 2014. A stalagmite record of abrupt climate change and possible westerlies-derived atmospheric precipitation during the Penultimate Glacial Maximum in northern China. Palaeogeogr. Palaeoclimatol. Palaeoecol. 393, 30–44.
Railsback, L.B., Gibbard, P.L., Head, M.J., Voarintsoa, N.R.G., Toucanne, S., 2015. An optimized scheme of lettered marine isotope substages for the last 1.0 million years, and the climatostratigraphic nature of isotope stages and substages. Quat. Sci. Rev. 111, 94–106.
Rohde, R.F., Hoffman, M.T., 2012. The historical ecology of Namibian rangelands: Vegetation change since 1876 in response to local and global drivers. Sci. Total Environ. 416, 276–288.
Romanek, C.S., Grossman, E.L., Morse, J.W., 1992. Carbon isotopic fractionation in synthetic aragonite and calcite: effects of temperature and precipitation rate. Geochim. Cosmochim. Acta 56, 419–430.
Rouault, M., Florenchie, P., Fauchereau, N., Reason, C.J.C., 2003. South east tropical Atlantic warm events and southern African rainfall. Geophys. Res. Lett. 30, 8009. http://dx.doi.org/10.1029/2002GL014840.
Russell, J.M., Johnson, T.C., 2005. Late Holocene climate change in the North Atlantic and equatorial Africa: millennial-scale ITCZ migration. Geophys. Res. Lett. 32, L17705. http://dx.doi.org/10.1029/2005GL023295.
Schefuß, E., Kuhlmmann, H., Mollenhauer, G., Prange, M., Pätzold, J., 2011. Forcing of wet phases in southeast Africa over the past 17,000 years. Nature 480, 509–512.
Schneider, T., Bischoff, T., Haug, G.H., 2014. Migrations and dynamics of the intertropical convergence zone. Nature 513, 45–53. http://dx.doi.org/10.1038/Nature13636.
Scussolini, P., Peeters, F.J.C., 2013. A record of the last 460 thousand years of upper ocean stratification from the central Walvis Ridge, South Atlantic. Paleoceanography 28, 426–439. http://dx.doi.org/10.1002/palo.20041.
Shakun, J., Lea, D.W., Lisiecki, L.E., Raymo, M.E., 2015. An 800-kyr record of global surface ocean $\delta^{18}O$ and implications for ice volume-temperature coupling. Earth Planet. Sci. Lett. 426, 58–68.
Siegel, F.R., Dort Jr., W., 1966. Calcite-aragonite speleothems from a hand-dug cave in northeast Kansas. Int. J. Speleol. 2, 165–169.
Singarayer, J.S., Burrough, S.L., 2014. Interhemispheric dynamics of the African rainbelt during the late Quaternary. Quat. Sci. Rev. 124 (2015), 48–67.
Sinha, A., Berkelhammer, M., Stott, L., Mudelsee, M., Cheng, H., Biswas, J., 2011. The leading mode of Indian Summer Monsoon precipitation variability during the last millennium. Geophys. Res. Lett. 38, 15703. http://dx.doi.org/10.1029/2011GL047713.
Sletten, H.R., Railsback, L.B., Liang, F., Brook, G.A., Marais, E., Hardt, B.F., Cheng, H., Edwards, R.L., 2013. A petrographic and geochemical record of climate change over the last 4600 years from a northern Namibia stalagmite, with evidence of abruptly wetter climate at the beginning of southern Africa's Iron Age. Palaeogeogr. Palaeoclimatol. Palaeoecol. 376, 149–162.
Srivastava, P., Brook, G.A., Marais, E., 2005. Depositional environment and luminescence chronology of the Hoarusib River Clay Castles sediments, northern Namib Desert, Namibia. Catena 59, 187–204.
Still, C.J., Berry, J.A., Collatz, G.J., DeFries, R.A., 2003. Global distribution of C3 and C4 vegetation: carbon cycle implications. Glob. Biogeochem. Cycles 17. http://dx.doi.org/10.1029/2001GB001807 (6-1–6.14).
Stone, A.E.C., Thomas, D.S.G., 2013. Casting new light on late Quaternary environmental and palaeohydrological change in the Namib Desert: a review of the application of optically stimulated luminescence in the region. J. Arid Environ. 93, 40–58.
Stone, A.E.C., Thomas, D.S.G., Viles, H.A., 2010. Late Quaternary palaeohydrological changes in the northern Namib Sand Sea: new chronologies using OSL dating of interdigitated aeolian and water-lain interdune deposits. Palaeogeogr. Palaeoclimatol. Palaeoecol. 288, 35–53.
Stone, A.E.C., Bateman, M.D., Thomas, D.S.G., 2015. Rapid age assessment in the Namib Sand Sea using a portable luminescence reader. Quat. Geochronol. 30, 134–140.
Stuut, J.-B.W., Prins, M.A., Schneider, R.R., Weltje, G.J., Jansen, J.H.F., Postma, G., 2002. A 300-kyr record of aridity and wind strength in southwestern Africa: inferences from grain-size distributions of sediments on Walvis Ridge, SE Atlantic. Mar. Geol. 180, 221–233.
Thomas, D.S.G., Brook, G., Shaw, R., Bateman, M., Haberyan, K., Appleton, C., Nash, D., McLaren, S., Davies, F., 2003. Late Pleistocene wetting and drying in the NW Kalahari: an integrated study from the Tsodilo Hills, Botswana. Quat. Int. 104, 53–67.
Thrailkill, J., 1971. Carbonate deposition in Carlsbad Caverns. J. Geol. 79, 683–695.
Truc, L., Chevalier, M., Favier, C., Cheddadi, R., Meadows, M.E., Scott, L., Carr, A.S., Smith, G.F., Chase, B.M., 2013. Quantification of climate change for the last 20,000 years from Wonderkrater, South Africa: implications for the long-term dynamics of the Intertropical Convergence Zone. Palaeogeogr. Palaeoclimatol. Palaeoecol. 386, 575–587.
Tyson, P.D., 1986. Climatic Change and Variability in Southern Africa. Oxford University Press, Cape Town.
Tyson, P.D., Odada, E.O., Partridge, T.C., 2001. Late Quaternary environmental change in southern Africa. S. Afr. J. Sci. 97, 139–150.
U.S. Central Intelligence Agency, 1986, Natural vegetation in Africa (map, 1:48,000,000).
UNEP, 2010. Africa Water Atlas. Division of Early Warning and Assessment (DEWA), United Nations Environmental Programme, Nairobi, Kenya.
van Heerden, J., Taljaard, J.J., 1998. Africa and surrounding waters. In: Koroly, D.J., Vincent, D.G. (Eds.), Meteorology of the Southern Hemisphere. Meteorological Monographs of the American Meteorological Society 27, pp. 141–174.
Veitch, J., 2002. Surface thermal characteristics of the Angola-Benguela Front (ABFZ) from analysis of 18 years of satellite data (Thesis) Department of Oceanography, University of Cape Town (48 p.).
Wang, P., 2009. Global monsoon in a geologic perspective. Chin. Sci. Bull. 54, 1113–1136.
White, F., 1983. The Vegetation of Africa. UNESCO, Paris.
Woodborne, S., Hall, G., Robertson, I., Patrut, A., Rouault, M., Loader, N.J., 2015. A 1000-year carbon isotope rainfall proxy record from South African baobab trees (*Adansonia digitata* L.). PLoS ONE 10 (5), e0124202. http://dx.doi.org/10.1371/journal.pone.0124202.